

Evaluation of Weather Research and Forecasting Model Predictions Using Micrometeorological Tower Observations

Prashant Kumar¹  · Bimal K. Bhattacharya² · P. K. Pal¹

Received: 17 May 2014 / Accepted: 30 June 2015 / Published online: 14 July 2015
© Springer Science+Business Media Dordrecht 2015

Abstract Here we assess the predictive skill of short-range weather forecasts from the Weather Research and Forecasting (WRF) model with the help of micrometeorological tower observations. WRF model forecasts at a 3-h temporal resolution and 5000-m spatial resolution are compared with ground observations collected at micrometeorological towers during the year 2011 over the Indian landmass. Results show good agreement between the WRF model forecast and tower observed surface temperature and relative humidity, 10-m wind speed, and surface pressure. The WRF model simulations of surface energy fluxes, such as incoming shortwave, longwave radiation, and ground heat flux are also compared with micrometeorological tower measurements. Relatively high errors in incoming shortwave radiation flux may be attributed to the lack of accurate cloud prediction and the non-inclusion of aerosol load. The cyclic pattern of errors in surface relative humidity is found to be tightly and oppositely coupled with the incoming longwave radiation flux. Errors in soil heat fluxes during daytime hours are dominated by errors in the incoming shortwave radiation flux.

Keywords Atmospheric surface layer · Micrometeorological observations · Model verification · Weather Research and Forecasting model

1 Introduction

The economy of a country depends on accurate and high resolution short-, medium- and long-range weather forecasts (Kumar et al. 2013a), used in agriculture, water resources, aviation, and disaster mitigation, on a daily basis (Strand 2000). Continuous verification of numeri-

✉ Prashant Kumar
kam3545@gmail.com; prashant22@sac.isro.gov.in

¹ Atmospheric Sciences Division, Atmospheric and Oceanic Sciences Group, Earth, Ocean, Atmosphere, Planetary Sciences and Applications Area, Space Applications Centre (ISRO), Ahmedabad 380015, India

² Crop Inventory and Agro-Ecosystems Division (CAD), ABHG, Space Applications Centre (ISRO), Ahmedabad 380015, India

cal weather prediction (NWP) models with observations from ground-based instruments is obligatory in evaluating the quality of model forecasts, and to provide feedbacks on improving the performance of numerical models. We have performed a number of studies (Kumar et al. 2011, 2013a, 2014a,b) on the verification of NWP model-predicted meteorological parameters (e.g. surface temperature, moisture, wind speed, and rainfall) with conventional observations. Quite a few earlier studies estimate errors in the predicted surface fluxes (e.g. Oncley and Dudhia 1995; Zamora et al. 2003; Cheng and Steenburgh 2005; Prabha and Hoogenboom 2010; Kumar et al. 2013a). Marciotto (2013) discussed the relation between the radiation budget and the ground heat flux, the energy stored in the soil, and the residual of the energy balance in urban and suburban areas of Oklahoma City, USA, together with the variability of the energy fluxes across the urban area. The evaluation over land surfaces of the flux parametrization in atmospheric models has been carried out by Beljaars and Holstag (1991), inter alia, while Mahura et al. (2009) investigated the effects of urban schemes in the HIRLAM numerical weather forecasting system. The surface energy fluxes obtained from the Weather Research and Forecasting (WRF) model simulations were evaluated by Jaksza (2012) for the Snake basin, while recent studies (Baker et al. 2013; Kleczek et al. 2014) have evaluated surface and upper-air parameters from WRF fine-scale model simulations. However, no dedicated study of the diurnal evaluation of NWP high-resolution fluxes have been made over diverse agro-climatic settings such as in India using micrometeorological measurements for different vegetative systems.

A network of 22 INSAT (Indian National SATellite System)-linked micrometeorological towers has been established across the country on the initiatives of the Indian Space Research Organization (ISRO) (Bhattacharya et al. 2009). Observations from micrometeorological towers provide a unique opportunity to validate model-predicted meteorological parameters as well as surface fluxes from the same platform. These tower observations may help improve the quality of the NWP model forecasts, and the description of land-surface characteristics in NWP models. The objective therefore is to validate several important surface parameters available from WRF model simulations against tower observations.

2 Micrometeorological Tower Data

A network of 10-m tall micrometeorological towers was installed under a national project titled “Energy and Mass Exchange in Vegetative Systems” under the aegis of the ISRO Geosphere-Biosphere Programme. These towers have instruments that measure the surface temperature, humidity, and wind speed at 30-min intervals at three vertical levels, soil temperature and soil moisture at three depths, two-depth soil heat fluxes, and shortwave and longwave radiation fluxes on a 30-min basis over different land-cover types across 15 broad agro-climatic zones (Bhattacharya et al. 2009, 2013b). The short vegetation surfaces include crops, grasses, natural shrubs, wetland vegetation, and young forest where the mean maximum canopy height varies from 1 to 2.5 m. Twenty-two micrometeorological towers were installed in India over 15 agro-climatic regions within the footprint of INSAT, each one with an optimal fetch of 500–1000 m, maintaining a fetch ratio of 1:50–1:100. These towers are spread over alluvial, black, red, grey-brown, and desert soils distributed across humid to arid climates. Soil temperature and moisture measurements are available at 0.05-, 0.1- and 0.2-m depths. The tower observations from 22 locations were collected through the data relay transponder on board the ISRO’s INSAT 3A satellite, with Yagi antenna attached to each tower transmitting observations of 26 data fields through four signal packets. Micrometeorological tower observations are archived in the Meteorological and Oceanographical

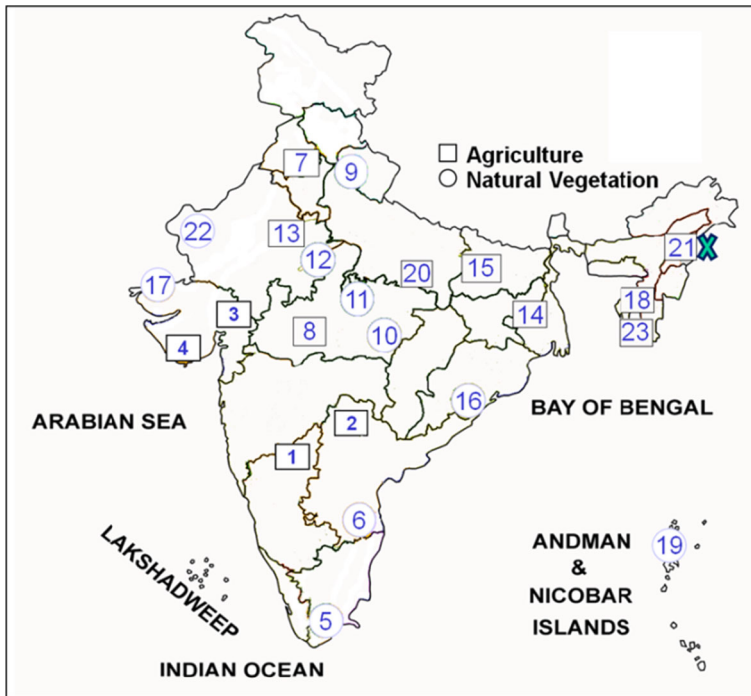


Fig. 1 Distribution of micrometeorological towers over the Indian region

Satellite Data Archival Centre (www.mosdac.gov.in) maintained by the Space Applications Centre of ISRO; the spatial distribution of ISRO micrometeorological towers is shown in Fig. 1. The prevailing cover types at tower locations and land-use/land-cover (LULC) types defined in the WRF model collocated to tower locations are summarized in Table 1. The match is quite good where the tower fetch footprint (500–1000 m) has similar surrounding extended land-cover types within the WRF model spatial resolution (5000 m). But mismatches arise at those tower locations where existing land-cover types in the tower fetch footprint are surrounded by different cover types within the WRF model grid.

The sensible and latent heat fluxes are generally estimated from the tower measurements either using the Bowen ratio energy balance approach assuming energy balance closure, or using the flux-profile method with aerodynamic assumptions. Both approaches have their inherent uncertainties thereby leading to errors in energy balance closure to $\pm 30\%$ (Bhat-tacharya et al. 2013a; Singh et al. 2014). Direct and improved measurements of the sensible and latent heat fluxes depend on the eddy-covariance approach, but in India, no systematic network of eddy-covariance sites exists.

3 Methodology and Model Description

3.1 Model Description

The Weather Research and Forecasting (Skamarock et al. 2008) model version 3.5 used herein is a limited area, non-hydrostatic, primitive equation model with multiple options for various

Table 1 Wide range of climate, soil, cover types represented by micrometeorological tower and corresponding land-use/land-cover used in WRF model

No.	Tower locations	Co-ordinates	Climate and soil	Tower cover types	WRF land-use/land-cover
1.	Bijapur, Karnataka	16.78°N, 75.75°E	Semi-arid/black	Rainfed cropland	Shrubland
2.	Hayathnagar, Hyderabad	17.34°N, 78.59°E	Semi-arid/black	Rainfed cropland	Dryland cropland and pasture
3.	Nawagam, Gujarat	22.79°N, 72.57°E	Semi-arid/grey-brown	Irrigated cropland	Cropland/grassland mosaic
4.	Junagadh, Gujarat	21.50°N, 70.45°E	Semi-arid/black	Irrigated cropland	Cropland/grassland mosaic
5.	Mahendragiri, TN	08.30°N, 77.56°E	Humid/red sandy	Shrubland	Irrigated cropland and pasture
6.	Sriharikota, AP	13.62°N, 80.23°E	Semi-arid/black	Shrubland	Irrigated cropland and pasture
7.	Naraingarh, Punjab	30.59°N, 76.26°E	Sub-humid/alluvial	Irrigated cropland	Irrigated cropland and pasture
8.	Powarkheda, MP	22.70°N, 77.75°E	Sub-humid/black	Irrigated cropland	Dryland cropland and pasture
9.	Dehradun, Uttarakhnad	30.33°N, 78.00°E	Sub-humid/mountain (red)	Coniferous forest	Irrigated cropland and pasture
10.	Kanha, MP	22.36°N, 80.58°E	Sub-humid/black	Moist grassland	Deciduous broadleaf forest
11.	Bandhavgarh, MP	23.92°N, 81.10°E	Sub-humid/black	Semi-moist grassland	Savanna
12.	Shivpuri, MP	25.44°N, 77.70°E	Sub-humid/black	Semi-dry grassland	Cropland/grassland mosaic
13.	Bharatpur, Rajasthan	27.20°N, 77.45°E	Semi-arid/alluvial	Irrigated cropland	Dryland cropland and pasture
14.	Chakdah, WB	23.06°N, 88.54°E	Sub-humid/alluvial	Irrigated cropland	Irrigated cropland and pasture
15.	Samastipur, Bihar	25.98°N, 85.67°E	Sub-humid/alluvial	Irrigated cropland	Dryland cropland and pasture
16.	Chilika, Orissa	19.71°N, 85.19°E	Humid/alluvial	Wetland vegetation	Cropland/grassland mosaic
17.	Bhuj, Gujarat	23.79°N, 69.51°E	Semi-arid/alluvial(sodic)	Dry grassland	Shrubland
18.	Kolasib, Mizoram	24.21°N, 92.68°E	Humid/red	Rainfed cropland	Mixed forest
19.	Diglipur, A & N	13.26°N, 93.00°E	Humid/alluvial	Rainfed cropland	Evergreen broadleaf
20.	Mirzapur, UP	25.04°N, 82.60°E	Sub-humid/alluvial	Shrubland	Irrigated cropland and pasture
22.	Jaisalmer, Rajasthan	26.99°N, 71.33°E	Arid/desert	Dry grassland	Barren or sparsely vegetated
23.	Hnahlan, Mizoram	23.53°N, 93.18°E	Humid/red	Rainfed cropland	Mixed forest

MP Madhya Pradesh, AP Andhra Pradesh, UP Uttar Pradesh, WB West Bengal, A & N Anadaman and Nicobar

physical parametrization schemes. This version employs Arakawa C-grid staggering for the horizontal grid and a fully compressible system of equations; a terrain-following hydrostatic pressure coordinates with vertical grid stretching is implemented vertically. The time-split integration uses a third-order Runge-Kutta scheme (Wicker and Skamarock 2002) with a smaller timestep for acoustic and gravity wave modes. The WRF model physical options used consist of the single moment 6-class simple ice scheme for microphysics (Lin et al. 1983); the Kain–Fritsch scheme (Kain 2004) for the cumulus convection parametrization, and the Yonsei University planetary boundary-layer scheme (Hong and Dudhia 2003). The rapid radiative transfer model (RRTM; Mlawer et al. 1997) and the Dudhia scheme (Dudhia 1989) are used for longwave and shortwave radiation, respectively. The Noah land-surface model (Chen and Dudhia 2001) is selected in this version of the WRF model, and contains four soil moisture layers, namely 0–0.1, 0.1–0.4, 0.4–1.0, and 1.0–2.0 m below the surface. The thicknesses of the lowest atmospheric layers are 75.8, 103.7, 132.4, 166.8, 212.3 and 260.2 m. Table 2 summarizes the various schemes used in the WRF model version.

The WRF model and its three-dimensional variational (3D-Var) data assimilation system (Barker et al. 2004) are configured and implemented to provide high spatial resolution (5000 m) short-range weather forecasts over India. WRF 3D-Var aims at producing an optimal estimate of the true atmospheric conditions by minimizing the cost function defined by

$$J(x) = (x - x^b)^T B^{-1} (x - x^b) + (y - H(x))^T (E + F)^{-1} (y - H(x)), \quad (1)$$

where x is the analysis state composed of atmospheric and surface variables and x^b is the first guess comprising values from the previous forecast. Conventional and satellite observations are represented by y , B and E represent the background and observation error covariance matrices respectively, and the observation operator H transforms the analysis to observation space $y = H(x)$. The inaccuracies introduced on account of the observation operator are contained in the representative error covariance matrix F . A detailed description of the 3D-Var system can be found in Barker et al. (2004).

3.2 Design of Experiment

The WRF model is integrated in a triple nested domain configuration (Fig. 2) with two-way nesting and a horizontal resolution of 45, 15 and 5 km over India with 260×235 , 352×373

Table 2 Summary of the selected WRF model schemes

WRF model options	Scheme selected for model run
1. Model version	WRF model version 3.5 (Skamarock et al. 2008)
2. Nesting	Two-way nesting
3. Horizontal grid	Arakawa C-grid
4. Integration scheme	Third-order Runge–Kutta method (Wicker and Skamarock 2002)
5. Microphysics	WSM 6-class graupel scheme (Lin et al. 1983)
6. Shortwave radiation	Dudhia scheme (Dudhia 1989)
7. Longwave radiation	RRTM scheme (Mlawer et al. 1997)
8. Land-surface model	Unified Noah land-surface model (Chen and Dudhia 2001)
9. Planetary boundary layer	Yonsei University YSU scheme (Hong and Dudhia 2003)
10. Cumulus parametrization	Kain–Fritsch scheme (Kain 2004)
11. Assimilation scheme	3D-Var method (Barker et al. 2004)

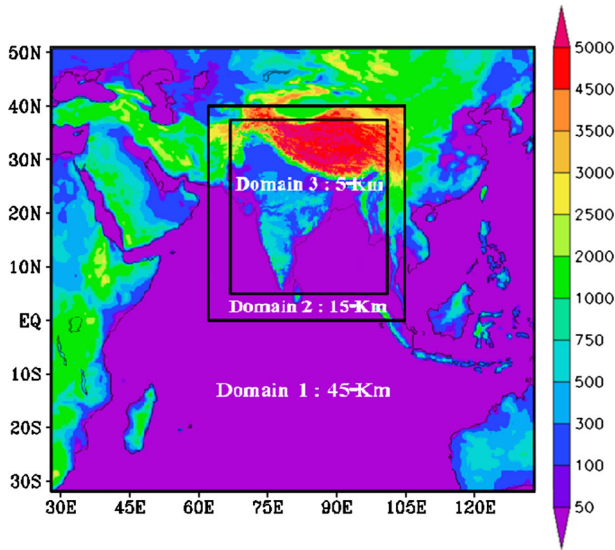


Fig. 2 The nested domain used in WRF model simulations

and 676×721 grid points in the x (longitude; east to west) and y (latitude; north to south) directions for domains 1, 2 and 3 respectively. The model has 36 vertical levels with the top of the model located at 10 hPa. The WRF model forecast is generated for the next 72 h initialized from 0000 UTC (0530 IST local standard time), with data available daily from satellites as well as conventional observations assimilated at the same time (here 0000 UTC) using 3D-Var data assimilation to improve the initial conditions of the WRF model (Kumar et al. 2011, 2014a; Singh et al. 2011). ISRO automatic weather stations, Oceansat-2 scatterometer (Kumar et al. 2013b) and advanced scatterometer winds, satellite retrieved temperature and moisture profiles, satellite radiances, refractivity, and conventional and satellite observations available from EUMETCast (European Organisation for the Exploitation of Meteorological Satellites (EUMETSAT)'s Multicast Distribution System) and National Centers for Environmental Prediction (NCEP) are used to improve the model initial conditions. The NCEP Global forecasting system (analysis and 6-h forecasts) is used to generate the initial and lateral boundary conditions of the WRF model. Hence, 3-hourly WRF model forecasts of air and soil temperatures, relative humidity, wind speed and atmospheric pressure at 5000-m spatial resolution throughout the year of 2011 (365 sample days) over the Indian region are compared against micrometeorological tower observations. The WRF model radiation and ground heat fluxes are compared with tower fluxes for a limited period November–December 2011 due to the availability of well-calibrated measured fluxes from the towers. The average measurement fetch for atmospheric sensors such as air temperature, relative humidity, wind speed, atmospheric pressure, incoming shortwave and longwave radiation at the micrometeorological towers is about 500 m. However, it is still less (about 50 m) for soil sensors such as soil temperature and ground heat flux. The tower data closest to the relevant WRF model grid point (here 5000 m) are directly compared without any interpolation.

4 Results and Discussion

In this study, mean error (*BIAS*) and root-mean-square difference (*RMSD*) are considered as the standard statistical measures to evaluate the quality of WRF model forecasts during the year 2011. WRF model analyses and 3-hourly forecasts of surface (2-m air) temperature and relative humidity, 10-m wind speed and direction, soil temperature, surface pressure, downward shortwave (S^{\downarrow}) and longwave (L^{\downarrow}) radiative fluxes at the surface, and ground heat flux (G_s) are compared with micrometeorological tower observations. The above three fluxes are direct measured quantities at the micrometeorological towers.

4.1 Temperature

BIAS and *RMSD* values for the WRF-model simulated surface temperature analyses and forecasts are compared with tower observations as shown in Fig. 3. The left (primary) y-axis shows the *RMSD* and the right (secondary) y-axis shows the *BIAS* statistics. Since these tower observations are not used in the data assimilation process, the verification can be considered as an independent validation. A gross quality control check is performed for validation, such that if the difference in the model forecast values and tower observations valid at the same time is more than 20 K, the corresponding points are discarded. This quality control is applied to avoid unrealistic cases, which may be due to signal interruption while transmitting data from the INSAT-3A data relay transponder to the ground receiving station. Approximately, 9 % of temperature data are discarded after this check. The *RMSD* and *BIAS* values of 2.6 and 0.5 K, respectively, are found in the WRF model analysis, which shows that the analysis itself has an error in the range of 2–3 K. The *RMSD* values remain below 4.2 K (Fig. 3) throughout the 72-h model run, but *RMSD* increases from ≈ 2.6 to ≈ 4.2 K as the forecast length increases. The *RMSD* values in temperature forecasts show a semi-diurnal cycle that has a local minimum in the 12-h forecasts (e.g. 12-h, 24-h etc.) compared to neighbouring forecast lengths. A positive *BIAS* value occurred at all forecast times, showing that the WRF model overestimated temperature when compared with tower observations.

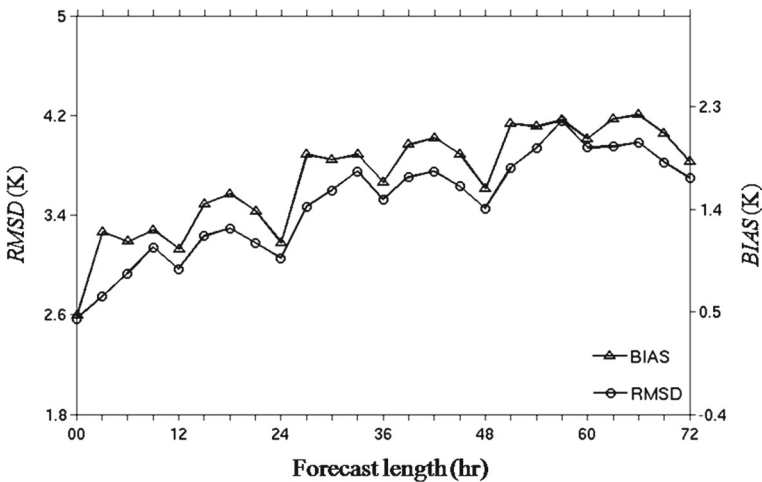


Fig. 3 Temporal distribution of *RMSD* and *BIAS* values in 3-h surface temperature forecasts during the year 2011 (total 365 sample days)

Table 3 Monthly statistics of 24-h WRF model forecast when compared with micrometeorological tower observations

Parameter	Statistics	Jan	Feb	Mar	Apr	May	Jun	Jul	Aug	Sep	Oct	Nov	Dec
Temperature (K)	<i>BIAS</i>	1.6	1.3	1.9	1.5	1.3	1.2	1.0	0.9	0.4	0.6	0.7	0.8
	<i>RMSD</i>	3.7	3.3	3.4	3.4	3.5	2.9	2.0	2.7	2.0	3.0	2.9	3.4
Relative humidity (%)	<i>BIAS</i>	-12.8	-12.6	-12.7	-9.6	-8.9	-7.6	-5.0	-4.7	-5.3	-7.8	-7.8	-6.5
	<i>RMSD</i>	25.6	23.5	24.4	20.2	20.4	17.8	13.3	12.4	14.7	21.0	21.4	23.4
Wind speed (m s ⁻¹)	<i>BIAS</i>	2.5	2.4	2.7	2.4	2.6	3.2	3.2	3.0	2.7	1.9	2.4	2.8
	<i>RMSD</i>	3.2	3.1	3.3	3.2	3.3	4.0	3.9	3.7	3.3	2.4	3.1	3.6
Surface pressure (hPa)	<i>BIAS</i>	3.1	2.2	1.6	1.1	0.9	-0.1	0.2	1.4	2.3	2.7	2.3	2.7
	<i>RMSD</i>	11.1	9.8	9.5	9.5	10.3	9.6	9.5	10.5	11.0	11.0	11.0	11.6

Additionally, monthly error statistics of surface temperature forecasts (Table 3) demonstrate that a slightly smaller *RMSD* value (<3.0 K) is observed during the Indian summer monsoon (June–September) period while larger *RMSD* value (>3.3 K) is found in the pre-monsoon periods in 24-h forecasts. During July and September 2011, minimum *RMSD* values (2 K) occur in the 24-h surface temperature forecast. Slightly larger *RMSD* and *BIAS* values are observed in the 48-h surface temperature forecast compared to the 24-h temperature forecast. The elevation differences in the WRF model grids and corresponding micrometeorological stations could also contribute to errors in the surface air temperature. Generally, elevation differences between micrometeorological stations and the corresponding WRF grid point lie within 4–35 m, which corresponds to approximately 0.02 to 0.2 K error in temperature. For the Dehradun station, having a 202-m elevation difference, this error is approximately 1.3 K.

4.2 Relative Humidity

The temporal distribution of *BIAS* and *RMSD* values of surface relative humidity (*RH*) analysis and forecasts are shown in Fig. 4. As with surface temperature, a gross quality control check is used for *RH* verification. If the difference between model-simulated *RH* and tower-observed *RH* values is more than 50 %, the corresponding points are discarded during error computation. The unrealistic values of data fields could be due to the perturbation of satellite transmission of any of the four signal packets that carry a total of 26 data fields of tower measurements to the data relay transponder. Approximately 30 % of data are discarded after this quality control. The model initial condition has *RMSD* and *BIAS* values of 18 and -9 %, respectively; *RMSD* varies from ≈16 % (in 9-h forecast) to ≈21 % (in 45-h forecast) as the forecast length is increased but remains below 22 % throughout the 72-h forecast. The *RH RMSD* values show a diurnal cycle with a minimum around 0900 UTC and an increase in the next 9 h (to 1800 UTC). The maximum variation occurred between 1200 and 1500 UTC. Similarly, *BIAS* values follow a diurnal cycle with the maximum difference between 1200 UTC and 1500 UTC and minimum *BIAS* values at 0900 UTC. A low *BIAS* value is found for all forecast lengths, which shows that the WRF model underestimates the tower-observed relative humidity. Higher *RH* values are predicted during July, August and September 2011 (figure not shown), which matches well with tower observations. Higher *RMSD* values (>20 %) are found during the pre- and post-summer monsoon periods (Table 3), while the Indian summer monsoon period (June–September) shows smallest *RMSD* values (<18 %) at 24-h.

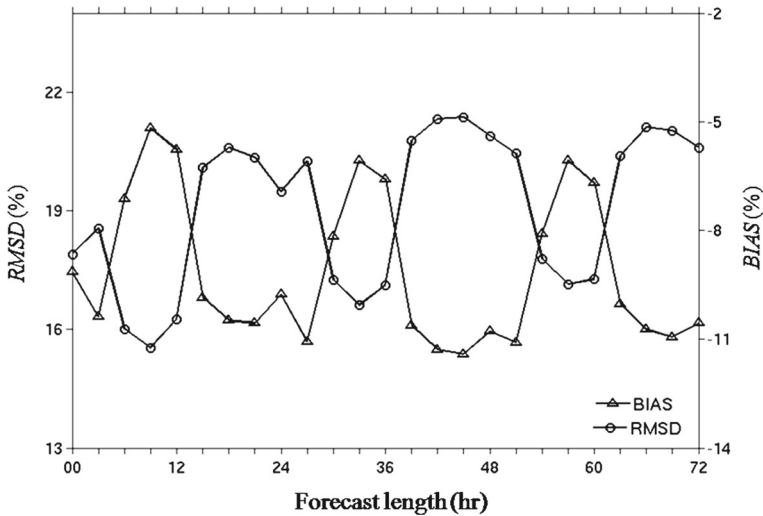


Fig. 4 Temporal distribution of *RMSD* (circle) and *BIAS* (triangle) in 3-hourly surface relative humidity (*RH*) forecast

4.3 Wind Speed

The prediction of surface wind is one of the most important but least accurate model derivatives over land. As with the forecast verification of surface temperature and relative humidity, a gross quality control is also applied for wind-speed forecast validation (Fig. 5). If the difference between two different wind speeds at any coincident time is $<30 \text{ m s}^{-1}$, the corresponding points ($\approx 40\%$ points are discarded) are considered for error calculation. *RMSD* values of $<3.9 \text{ m s}^{-1}$ are found at all forecast lengths based on one year's data, while *BIAS* values in the wind-speed forecast lie between 1 and 3 m s^{-1} . A slight increase is observed in 48-h and 72-h forecasts compared to 24-h forecasts. The maximum *BIAS* and *RMSD* values occur at around 1800 UTC and the minimum *RMSD* values occur at 0600 UTC. The WRF model overestimates the tower-observed wind speed in all months. *RMSD* values of approximately 4 m s^{-1} are found in 24-h wind-speed forecasts in June and July (Table 3), with minimum *RMSD* values found in October.

4.4 Surface Pressure

RMSD and *BIAS* values for the surface pressure analysis and forecasts are shown in Fig. 6a. *RMSD* values of $<11 \text{ hPa}$ are found in the surface pressure analysis and subsequent forecasts. *RMSD* values decrease by approximately 5% around 1200 UTC but higher *RMSD* values are found for all forecast lengths. *BIAS* values of less than 2 hPa are observed at all the forecast lengths. *RMSD* values of approximately 11 hPa are found in 24-h surface pressure forecasts for all months (Table 3). WRF model grids (5000 m) represent the average elevation using 1000-m elevation data from the United States Geological Survey, whereas, tower observations represent the point location. Errors in WRF model surface pressure forecasts may thus partly be due to these elevation mismatches. For 4–35 m deviation in elevation, surface pressure errors are approximately $0.5\text{--}5 \text{ hPa}$. One station located at Dehradun (the high topographic region) shows a large difference between the elevations (202 m), which represents a deviation of approximately 25 hPa in surface pressure.

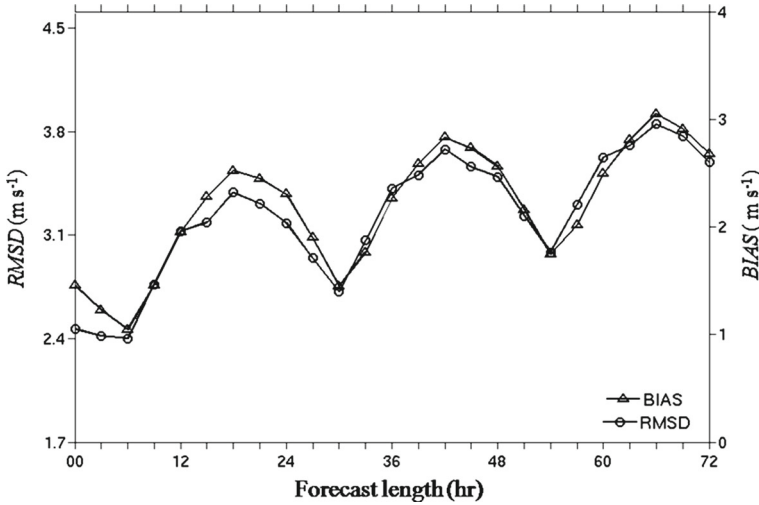


Fig. 5 Temporal distribution of *RMSD* (circle) and *BIAS* (triangle) values in 3-h surface (10-m) wind-speed forecast

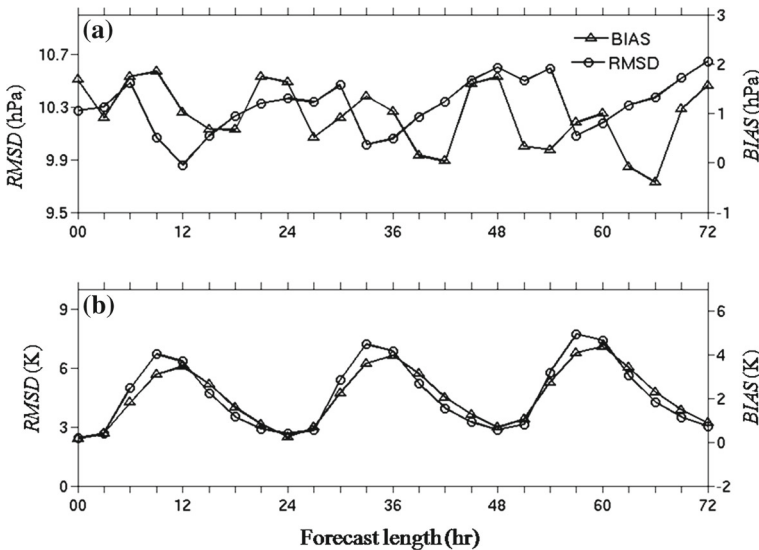


Fig. 6 Temporal distribution of *RMSD* (circle) and *BIAS* (triangle) in 3-h **a** surface pressure and **b** soil temperature forecast

4.5 Soil Temperature

The *RMSD* and *BIAS* values for soil temperature analyses and forecasts are shown in Fig. 6b. A slightly higher error occurs in soil temperature forecasts compared to surface temperature forecasts. The WRF model simulation is obtained for the soil temperature within the zero to 0.1 m depths beneath the soil surface, which compares with tower-observed soil temperature within zero to 0.05 m. In this soil layer, the vertical temperature gradient is greater during the

day than at night and varies according to soil type, soil moisture status and cover types. During the noon to afternoon hours in cloudless skies this gradient generally remains higher than the vertical gradient in air temperature. In addition, the measurement footprint of soil sensors at towers is much less than that of atmospheric sensors. The above factors may attribute to greater errors in soil temperature than in surface air temperature. Soil temperature forecasts have maximum and minimum errors at 0900 UTC and 0000 UTC, respectively. Negligible shifts are seen in 48-h and 72-h forecasts compared to the 24-h forecast. The impact of soil moisture errors on the diurnal simulation of the 0.05-m soil temperature, from a simple one-layer slab model, were evaluated for model initialization with observed soil temperatures at Watonga in the Oklahoma mesonet site (Godfrey and Stensrud 2008). It was reported that negative soil moisture *BIAS* values alone accounted for more than 1.6 K increase (or decrease) in the maximum (or the minimum) soil temperatures depending on the time of initialization. Positive soil moisture *BIAS* values accounted for a more modest reduction of almost 0.9 K in the amplitude of the diurnal soil temperature cycle. While underestimates of soil moisture may contribute to the sign of the soil temperature errors, soil moisture alone apparently cannot account for the magnitude of the errors in soil temperature.

4.6 Radiation Fluxes

4.6.1 Downward Shortwave

The scatter plot of the WRF model predicted downward shortwave radiative fluxes (S^{\downarrow}) and micrometeorological tower-observed incoming shortwave radiative fluxes at 0300, 0600, 0900 and 1200 UTC shows large (Fig. 7) positive *BIAS* (88 W m^{-2}) and *RMSD* (167 W m^{-2}) values over a limited period (November and December 2011). Four data clusters representing morning, midday, early afternoon and late afternoon hours, respectively are found in Fig. 7, and *RMSD* values of approximately 81, 205, 228 and 60 W m^{-2} are found in morning, midday, early afternoon and late afternoon hours, respectively. High positive *BIAS* values are found at midday (128 W m^{-2}) and early afternoon (165 W m^{-2}) compared to morning (-1 W m^{-2}) and late afternoon (46 W m^{-2}). The low insolation regime may be either due to low shortwave fluxes in the morning in cloudless situations, or due to cloudy conditions. The uncertainties in predicting cloud and fog dynamics may be the major reason for this scatter. The aerosol load generally remains higher during the latter part of the morning for weekdays due to higher pollution loads (Backman et al. 2012). However, observations of surface aerosol concentration do not necessarily relate to total column aerosols. For example, the boundary-layer height is lower in the morning compared to the afternoon. So, equivalent amounts of aerosols will produce larger surface concentrations in the morning even though their radiative impact is the same. In Fig. 7, points lying along the diagonal represent the smallest aerosol loading in the morning (0300 UTC). During midday (0600 UTC) and early afternoon (0900 UTC), points cluster along a line (above the diagonal) with a shallow slope, where aerosol attenuation is larger compared to 0300 UTC, and it is larger when the incoming radiation is weaker (for the same time of day, this corresponds to a shallower sun angle and hence a longer atmospheric path length). In late afternoon (1200 UTC), the departure from the diagonal is the largest, though the net radiative effect is small due to the weak radiative intensities. The lack of representation of aerosol characterization is a major drawback of the WRF model, and so a lack of attenuation of shortwave radiative flux due to aerosol loading in the insolation regime could lead to higher predicted fluxes compared to tower measurements.

The incoming shortwave radiative flux is the major energy input in the surface radiation and energy balance. The WRF downward shortwave radiative flux forecasts depend on

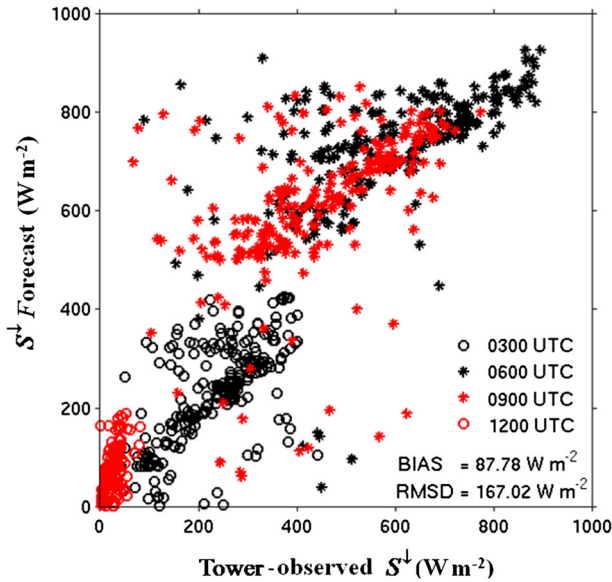


Fig. 7 Scatter plot of downward shortwave radiative flux (S^{\downarrow}) forecast from the WRF model and micrometeorological tower observed S^{\downarrow} radiation during November and December 2011

the cumulus parametrization scheme, which in turn is sensitive to surface relative humidity. Moreover, the roles of aerosol and Rayleigh scattering, and direct–diffuse irradiance partitioning have not been accounted for the WRF model for computing downward shortwave radiation. The prediction of cloud type and cloud-cover fraction from the atmospheric humidity profile is also a great source of uncertainty. The sensitivity of incoming shortwave radiation to aerosol optical depth in cloudless skies is shown by [Bhattacharya et al. \(2013b\)](#). In cloudy-sky conditions, the cloud-top albedo is the major determinant for attenuation of irradiances for the wavelength range of 300–750 nm ([Stephens 1978](#)), but both reflection and cloud absorption attenuate irradiances for wavelengths beyond 750 nm.

4.6.2 Downward Longwave

The 24-h WRF model predicted longwave radiative fluxes are compared with tower-observed incoming longwave fluxes in [Fig. 8](#). A diurnal pattern is noted with *RMSD* (*BIAS*) values that gradually increase (decrease) from 3 h and attain a peak (lowest point) at 6 h followed by a decrease (increase) towards 24 h. The minimum *RMSD* values gradually increase from day 1 to day 3, while the maximum *RMSD* values change very little. The 1:1 scatter plots of the WRF model predicted L^{\downarrow} and tower-observed L^{\downarrow} for November and December 2011 show *RMSD* values of 33 and 40 W m^{-2} and *BIAS* of -22 and -21 W m^{-2} . The cyclic patterns of *BIAS* and *RMSD* values of L^{\downarrow} are quite similar to relative humidity but are opposite in nature. It is known that incoming longwave radiative flux depends on sky temperature and air emissivity. The latter is greatly influenced by actual vapour pressure. Relative humidity is the ratio of the actual vapour pressure and air temperature-dependent saturation vapour pressure, while L^{\downarrow} is directly proportional to the product of sky temperature and air emissivity. Therefore, the nature of errors for both temperature and actual vapour pressure may influence differently values of L^{\downarrow} and *RH*.

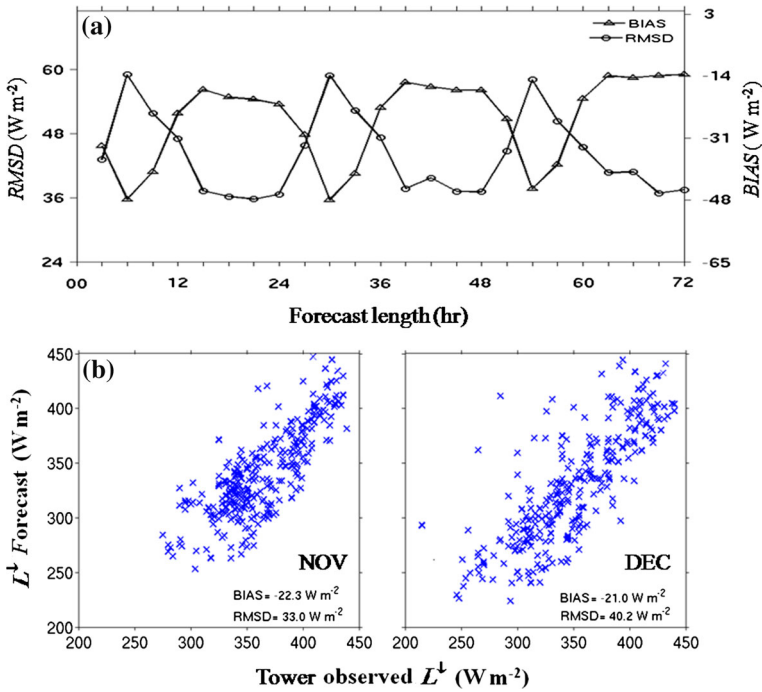


Fig. 8 a Temporal distribution of *RMSD* (circle) and *BIAS* (triangle) values in the 3-h downward longwave radiative flux (L^\downarrow) and b scatter plot of 24-h WRF L^\downarrow forecast and micrometeorological tower observed L^\downarrow during November and December 2011

4.7 Ground Heat Flux

Both *RMSD* and *BIAS* values of the WRF model predicted G_S show prominent cyclic patterns (Fig. 9). The inward and outward nature of G_S change with respect to day and night soil hydro-thermal regimes. The sign of the *BIAS* values depends on the sign of the ground heat flux. There is practically no increase or decrease in the magnitude of the minimum and maximum values of *BIAS* and *RMSD* as the forecast length increases up to 72 h. Depending on the time of day, *RMSD* values range from 47 to 113 W m⁻² and *BIAS* ranges from -103 to 62 W m⁻². The scatter plots of the WRF model predicted and tower-observed G_S at 24 h in the months of November and December 2011 show that there is a general overestimation by the WRF model leading to positive *BIAS* values of 31, 30 W m⁻² and *RMSD* values of 48, 50 W m⁻², respectively. The scatter plots are broad in nature as compared to the narrow-spread scatter plots for L^\downarrow .

4.8 Comparison of Errors of G_S in Relation to Other Parameters

The nature of variation of *RMSD* and *BIAS* values with forecast lengths are similar in both G_S and L^\downarrow , the latter shows negative *BIAS* values for all forecast lengths and the former shows *BIAS* values ranging from negative to positive. On the other hand, predicted soil temperature consistently shows positive *BIAS* values. At equilibrium, the ground heat flux is in balance with the soil temperature gradient, and the surface radiation budget in terms of net radiation,

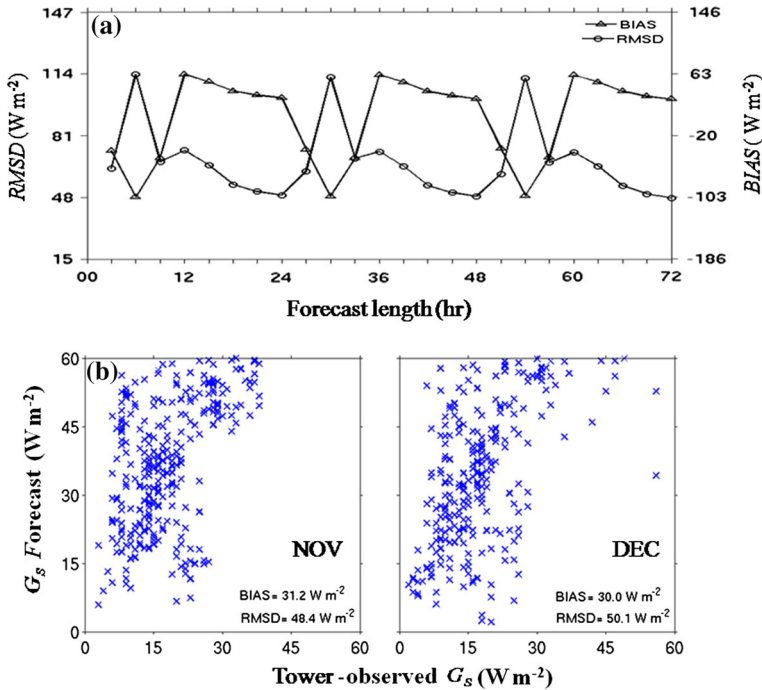


Fig. 9 a Temporal distribution of *RMSD* (circle) and *BIAS* (triangle) in 3-h G_S and b scatter plot of 24-h WRF model G_S forecast and micrometeorological tower-observed G_S during November and December 2011

sensible and latent heat fluxes. Both longwave and shortwave radiative fluxes govern net radiation with more contribution of the latter during daytime hours than the former.

The errors are relatively high in G_S compared to L^\downarrow . The latter is generally governed by atmospheric humidity, sky conditions, and atmospheric temperature, which have less spatial variability within a model grid resolution of 5 km. In contrast, the G_S is mainly influenced by the soil hydro-thermal regimes depending on thermal conductivity and heat capacity based on soil composition and structure, and also fractional vegetation cover above the soil. These factors might produce a greater spatial variability in G_S within a WRF model grid. The error statistics for G_S are expected to show more variability within the WRF model grid than L^\downarrow , but due to the relatively static nature of soil thermal conductivity and heat capacity over shorter times scales no shift was noticed in the minimum and maximum values of *BIAS* and *RMSD* in G_S , but a small shift is noticed for L^\downarrow with increase in the forecast length. Moreover, very little to no shift in the predicted soil temperature with increase in forecast length, but with increasing *BIAS* and *RMSD* values, are noticed for surface air temperature that might lead to no shift in the errors for G_S but a shift in the errors for L^\downarrow .

5 Conclusions

Short-range weather forecasts from the WRF model are compared with both surface weather and boundary-layer quantities such as shortwave, longwave and soil heat fluxes from micrometeorological towers over the Indian landmass for the first time. The tower network is important for quantifying the errors in the forecast of both weather and surface fluxes thus

establishing the need to improve the model deficiencies. Large errors in the incoming shortwave radiation flux suggest a need for improved representation of clouds and the inclusion of aerosol loading for attenuation of the shortwave flux in cloudless situations. The diurnal pattern of errors in relative humidity is found to be oppositely correlated to that of the incoming longwave radiation flux. The *BIAS* values in ground heat fluxes during daytime hours are possibly dominated by the *BIAS* values in incoming shortwave radiation flux apart from other possibilities. During nighttime, the *BIAS* values in ground heat fluxes are possibly influenced by *BIAS* values in incoming longwave radiation and soil temperature. The sources of forecast errors in WRF model could be many. One source of error is a gross mismatch between representations in land-cover types by the WRF model and the micrometeorological towers. The latter of course represent local-scale cover type while the WRF model considers aggregated cover type corresponding to the model grid resolution (5 km). In addition, there are elevation differences between the WRF model grids and the collocated towers that could contribute to errors in surface temperature and surface pressure. Moreover, systematic and direct measurements of sensible and latent heat fluxes from a network of eddy-covariance systems or scintillometers could be used to evaluate model-predicted turbulent heat fluxes at the present scale of study.

Acknowledgments The present study has been carried out under ISRO-GBP project titled “Energy and Mass Exchange in Vegetative Systems”. The authors would like to thank Mr. A. S. Kiran Kumar, Director, SAC for constant encouragement and guidance. The authors are also thankful to the National Center for Atmospheric Research (NCAR) for provision of the WRF model and to CDAC National PARAM Supercomputing Facility (NPSF) for running the WRF model at high resolution. The global analyzed and forecast data provided by National Centers for Environmental Prediction (NCEP) are acknowledged with sincere thanks and we are thankful to MOSDAC team for making the micrometeorological tower data available. The authors also thank anonymous reviewers for their guidance.

References

- Backman J, Rizzo LU, Hakula J, Nieninen J, Manninen HE, Morais F, Alto PP, Siivola E, Carbone S, Hillamo R, Artano P, Virkkula A, Petaja T, Kulmala M (2012) On the diurnal cycle of urban aerosols, black carbon and the occurrence of new particle formation events in springtime São Paulo, Brazil. *Atmos Chem Phys* 12:11733–11751
- Baker KR, Miseneris C, Obland MD, Ferrare RA, Scarino AJ, Kelly JT (2013) Evaluation of surface and upper air fine scale WRF meteorological modeling of the May and June 2010 CalNex period in California. *Atmos Environ* 80:299–309
- Barker DM, Huang W, Guo YR, Bourgeois AJ, Xiao QN (2004) A three-dimensional variational data assimilation system for MM5: implementation and initial results. *Mon Weather Rev* 132:897–914
- Beljaars ACM, Holstag AAM (1991) Flux parameterization over land surfaces for atmospheric models. *J Appl Meteorol* 30:327–341
- Bhattacharya BK, Dutt CBS, Parihar JS (2009) INSAT uplinked Agro-met Station—a scientific tool with a network of automated micrometeorological measurements for soil–canopy–atmosphere feedback studies. Paper No. TS9.1, ISPRS Archives XXXVIII-8/W3 workshop proceedings: impact of climate change on agriculture, pp 72–77. http://www.isprs.org/proceedings/XXXVIII/8-W3/B1/11-23_F.pdf
- Bhattacharya BK, Singh N, Bera N, Nanda MK, Bairagi GD, Raja P, Bal SK, Murugan V, Kandpal BK, Patel BH, Jain A, Parihar JS (2013a) Canopy-scale dynamics of radiation and energy balance over short vegetative systems. Report No. SAC/EPISA/ABHG/IGBP- EMEVS/SR/02/2013. Scientific Report, Space Applications Centre, India, pp 1–72
- Bhattacharya BK, Padmanabhan N, Sazid Md, Ramakishna R, Parihar JS (2013b) Assessment of solar energy potential over India using diurnal remote sensing observations using Indian geostationary satellite data. *Int J Remote Sens* 34(20):7069–7090
- Chen F, Dudhia J (2001) Coupling an advanced land-surface/ hydrology model with the Penn State/ NCAR MM5 modeling system. Part I: Model description and implementation. *Mon Weather Rev* 129:569–585

- Cheng WYY, Steenburgh WJ (2005) Evaluation of surface sensible weather forecasts by the WRF and the Eta Models over the Western United States. *Weather Forecast* 20:812–821
- Dudhia J (1989) Numerical study of convection observed during the winter monsoon experiment using a mesoscale two-dimensional model. *J Atmos Sci* 46:3077–3107
- Godfrey CM, Stensrud DJ (2008) Soil temperature and moisture errors in operational Eta Model analyses. *J Hydrometeorol* 9:367–387
- Hong SY, Dudhia J (2003) Testing of a new non-local boundary layer vertical diffusion scheme in Numerical weather prediction applications. In: 20th Conference on weather analysis and forecasting/16th conference on numerical weather prediction, vol 17. American Meteorological Society Session, Seattle, WA
- Jaksa WTA (2012) Assessing the surface energy balance components in the snake river basin. PhD Thesis, Master of Science in Civil Engineering, Boise State University
- Kain JS (2004) The Kain-Fritsch convective parameterization: an update. *J Appl Meteorol* 43:170–181
- Kleczek MA, Steeneveld GJ, Holtslag AAM (2014) Evaluation of the weather research and forecasting mesoscale model for GABLS3: impact of boundary-layer schemes, boundary conditions and spin-up. *Boundary-Layer Meteorol* 152:213–243
- Kumar P, Singh R, Joshi PC, Pal PK (2011) Impact of additional surface observation network on short range weather forecast during summer monsoon 2008 over Indian subcontinent. *J Earth Syst Sci* 120:1–12
- Kumar P, Bhattacharya BK, Pal PK (2013a) Impact of vegetation fraction from Indian geostationary satellite on short-range weather forecast. *Agric For Meteorol* 168:82–92
- Kumar P, Kumar KPH, Pal PK (2013b) Impact of Oceansat-2 scatterometer winds and TMI observations on PHET cyclone simulation. *IEEE Trans Geosci Remote Sens* 51(6):3774–3779
- Kumar P, Kishtawal CM, Pal PK (2014a) Impact of satellite rainfall assimilation on Weather Research and Forecasting model predictions over the Indian region. *J Geophys Res Atmos* 119(5):2017–2031
- Kumar P, Bhattacharya BK, Nigam R, Kishtawal CM, Pal PK (2014b) Impact of Kalpana-1 derived land surface albedo on short-range weather forecasting over Indian region. *J Geophys Res Atmos* 119(6):2764–2780
- Lin YL, Farley RD, Orville HD (1983) Bulk parameterization of the snow field in a cloud model. *J Clim Appl Meteorol* 22:1065–1092
- Mahura A, Baklanov A, Petersen C, Nielsen NW, Amstrep B (2009) Verification and case studies for urban effects in HIRLAM numerical weather forecasting. Meteorological and air quality models for urban areas. Springer, Berlin, pp 143–150
- Marciocto ER (2013) Variability of energy fluxes in relation to the net-radiation of urban and suburban areas: a case study. *Meteorol Atmos Phys* 121:17–28
- Mlawer EJ, Taubman SJ, Brown PD, Iacono MJ, Clough SA (1997) Radiative transfer for inhomogeneous atmosphere: RRTM, a validated correlated-k model for the longwave. *J Geophys Res* 102:16663–16682
- Oncley SP, Dudhia J (1995) Evaluation of surface fluxes from MM5 using observations. *Mon Weather Rev* 123:3344–3357
- Prabha T, Hoogenboom G (2010) Evaluation of solar irradiance at the surface inferences from in situ and satellite observations and a mesoscale model. *Theor Appl Climatol* 102:455–469
- Singh R, Kumar P, Pal PK (2011) Assimilation of Oceansat-2 Scatterometer derived surface winds in the weather research and forecasting model. *IEEE Trans Geosci Remote Sens* 50(4):1015–1021
- Singh N, Patel NR, Bhattacharya BK, Soni P, Parida BR, Parihar JS (2014) Analyzing the dynamics and inter-linkages of carbon and water fluxes in subtropical pine (*Pinus roxburghii*) ecosystem. *Agric For Meteorol* 197:206–218
- Skamarock WC, Klemp JB, Dudhia J, Gill DO, Barker DM, Duda MG, Huang XY, Wang W, Powers JG (2008) A description of the Advanced Research WRF, Version 3. NCAR/TN-475 STR; NCAR Technical Note, Mesoscale and Microscale Meteorology Division, National Center of Atmospheric Research, 113 pp
- Stephens GL (1978) Radiation profiles in extended water clouds. II: parameterization schemes. *J Atmos Sci* 35:2123–2132
- Strand JF (2000) Some agrometeorological aspects of pest and disease management for the 21st century. *Agric For Meteorol* 103:73–82
- Wicker LJ, Skamarock WC (2002) Time splitting methods for elastic models using forward time schemes. *Mon Weather Rev* 130:2088–2097
- Zamora RJ, Solomon S, Dutton EG, Bao JW, Trainer M, Portmann RW, White AB, Nelson DW, McNider RT (2003) Comparing MM5 radiative fluxes with observations gathered during the 1995 and 1999 Nashville southern oxidants studies. *J Geophys Res* 108:4050